Full length article

Hydrogen-based direct reduction of combusted iron powder: Deep pre-oxidation, reduction kinetics and microstructural analysis

Laurine Choisez [a,*], Kira Hemke [b], Özge Özgün [b], Claudio Pistidda [c], Henrik Jeppesen [d], Dierk Raabe [b], Yan Ma [b]

[a] Institute of Mechanics, Materials and Civil Engineering, IMAP, UCLouvain, Place Sainte 2, Louvain-la-Neuve B-1348, Belgium
[b] Max-Planck-Institut für Eisenforschung, Max-Planck-Str. 1, Düsseldorf 40237, Germany
[c] Helmholtz-Zentrum Hereon, Max-Planck-Straße 1, Geesthacht 21502, Germany
[d] Deutsches Elektronen-Synchrotron (DESY), Notkestrasse 85, Hamburg 22607, Germany

ARTICLE INFO

ABSTRACT

Iron powder can be a sustainable alternative to fossil fuels in power supply due to its high energy density and abundance. Iron powder releases energy through exothermic oxidation (combustion), and stores back energy through its subsequent hydrogen-based reduction, establishing a circular loop for renewable energy supply. Hydrogen-based direct reduction is also gaining global momentum as possible future backbone technology for sustainable iron and steel production, with the aim to replace blast furnaces. Here, we investigate the microstructural formation mechanisms and reduction kinetics behind hydrogen-based direct reduction of combusted iron powder at moderate temperatures (400–500 °C) using thermogravimetry, *ex-situ* X-ray diffraction, scanning electron microscopy coupled with energy dispersive spectroscopy and electron backscatter diffraction, as well as *in-situ* high-energy X-ray diffraction. The influence of pre-oxidation treatment was studied by reducing both ascombusted iron powder (50 % magnetite and 50 % hematite) and the same powder after pre-oxidation (100 % hematite). A gas diffusion-limited reaction was obtained during the *in-situ* high-energy X-ray diffraction experiment, with successive hematite and magnetite reduction, and a strong increase in reduction kinetics with initial hematite content. Faster reduction kinetics were obtained during the thermogravimetry experiment, with simultaneous hematite and magnetite reduction. In this case, the reduction reaction was limited by a mix of phase boundary and nucleation and growth models, as analyzed by multi-step model fitting methods as well as by microstructural investigation. When not limited by gas diffusion, the pre-oxidation treatment showed almost no influence on the reduction time but a strong effect on the final microstructure of the reduced powder.

1. Introduction

Decarbonization of the storage and consumption of energy is urgently required to combat global warming, as it accounts for more than 70 % of global greenhouse gas emissions due to the use of fossil fuels [1]. Sustainable energy carriers and storage technologies are key to this transition to overcome the spatiotemporal intermittence of sustainable energy production based on solar, wind, hydropower, and geothermal energies. Metal fuels have therefore been introduced as carbon-free, energy-dense, and sustainable energy carriers [2]. In particular, iron powder is suited for this purpose due to its low cost, safety, abundance, and straightforward retrofitting of existing power plants [2–4]. In this concept, heat is generated by the combustion of the iron powder, *i.e.*, its

high-temperature exothermic oxidation, producing iron oxide particles as a product of the reaction. The pure iron particles can then subsequently be recovered by reducing the combustion products using reducing gasses, such as H_2 or CO. Particularly, hydrogen-based direct reduction (HyDR) is highly attractive for this fuel recycling step. Potentially, this sustainable process does not emit any CO_2 emission for the whole energy cycle when the hydrogen is produced from renewable energy sources. In addition, the particles stay in the solid state during this reduction process, thus no additional atomization process is required (which is the case after liquid-state reduction).

Such a HyDR step of combusted iron powder for a carbon-free energy sector shows many similarities to the currently globally pursued hydrogen-based ironmaking approaches [5,6]. HyDR is overall an

* Corresponding author.
  E-mail address: laurine.choisez@uclouvain.be (L. Choisez).

endothermic reaction, requiring a larger energy input to maintain the temperature in the reactor, compared to the exothermic CO-based reduction [6]. However, the former shows systematically faster reduction kinetics, up to five times faster [7], compared with the use of CO. Direct reduction has been mostly studied on iron ores in the form of pellets (>1 mm) [8–17] and fines (<1 mm) [14,16,18–22], and more rarely on pure iron oxide fines [23–26] and single crystals [27–29]. Due to the different experimental set-ups and features of iron ores (in terms of ore type, shape, size, microstructure, chemical composition, porosity, *etc.*), the kinetics and mechanisms dominating the HyDR are not consistent in the literature for the case of iron ores [13], not even for iron oxide powder with high purity [30]. An increase in the HyDR kinetics is generally observed with an increase in the hydrogen pressure and the reduction temperature [10,14,31,32]. However, a decrease in the kinetics and final reduction level has been observed around 650–900 °C during the reduction of iron oxide single crystals, compact oxides and fines [16,22,31,33]. These decreases are presumably due to local iron sintering around unreduced wüstite islands [7,16–18,22,33], and/or to the severe sintering of the iron oxide fines [31], slowing down in both cases the inward diffusion of hydrogen or outward diffusion of oxygen [7,16–18,22,33]. Below 570 °C, the reduction of iron oxide is facilitated by the direct reduction from magnetite to α-iron, by-passing the more sluggish reduction step from wüstite to α-iron [34], where wüstite is thermodynamically unstable. In addition, pre-treatment of iron ores in the form of a pre-oxidation step prior to the subsequent reduction has been found to affect the HyDR kinetics. The full pre-oxidation of iron ores to hematite is sometimes referred to as "deep oxidation" in the literature [21,35], as opposed to a partial pre-oxidation. In the framework of iron as a sustainable fuel, the complete oxidation of iron to hematite during the combustion process is aimed for exploiting a maximum of the stored heat through the oxidation process and get as close as possible to the thermodynamic limit of energy storage efficiency. Yet, experimentally, the combustion products obtained are not fully oxidized but composed of a mix of hematite and magnetite phases [36]. Nevertheless, the oxidation of iron to a mix of 50 % magnetite and 50 % hematite corresponds to 95 % of the heat potential of iron [37]. Completely oxidizing the combusted products to 100 % hematite could increase the overall energy efficiency by recovering the last 5 % of stored energy and by accelerating the HyDR kinetics. Deep pre-oxidation of magnetite ores has been observed to strongly increase their subsequent HyDR kinetics, due to the formation of micro-cracks [38], an increase in open porosity [15], and phase-transformation-induced microstructure refinement [37]. Enhanced reducibility of magnetite ores was found for a pre-oxidation step conducted in a temperature range of 700–900 °C by Chen et al. [15] and of 800–1000 °C by Monsen [37]. Zheng et al. [22] also investigated the influence of the pre-oxidation temperature and oxidation level of magnetite ores on the ensuing HyDR. Increasing the oxidation temperature from 800 °C to 1000 °C was reported to strongly decrease the specific surface area of the particles, presumably due to local sintering of the particles, improving the fluidization of the particles but decreasing its reduction kinetics [22].

After combustion, the microstructure and porosity of the combusted iron particles differ strongly from those of natural iron ores, affecting the reduction behavior. The combustion process produces spherical particles possessing a large range of pore sizes, ranging from a few nanometers to hundreds of micrometers (up to 80 % of the particle diameter) [36]. As all these factors affect reduction kinetics and the overall efficiency of iron powder as an alternative fuel, it is important to investigate the HyDR of combusted powder to comprehend the underlying fundamental transport and transformation mechanisms. Hessels et al. [31] studied the kinetics of HyDR of combusted iron powder in the temperature range of 400–900 °C in hydrogen at a pressure of 0.25–1 atm. This study brought important insights into the reduction process and concluded that the reduction process was dominated by a phase boundary reaction in the temperature range of 400–500 °C, with a transition from phase boundary reaction to nucleation and growth

dominated reduction in the range of 600–900 °C. Their study was based on the analysis of the reduction kinetic curves obtained by thermogravimetry analysis [31]. Many additional insights on the fundamental mechanisms governing the reduction process can be gained from a microstructural analysis of the partially and fully reduced particles, as conducted in this work. Moreover, the microstructure and porosity distribution of the reduced iron particles will strongly impact the subsequent combustion process. The combustion process starts by igniting the iron particles, *i.e.*, a self-sustained thermal runaway process. The ignition temperature must be well controlled: as small as possible to minimize the input energy required to start the combustion process, but must be also large enough to avoid flammability issues. The ignition temperature is given by the balance between the heat rate produced by the solid-state oxidation of the reduced iron particles and the heat exchange rate with the surrounding gas [39,40]. Both phenomena depend on the surface area of the reduced iron particles, given by the final particle size and porosity size distribution [39,40]. Therefore, such features are particularly important to investigate in the framework of a closed sustainable metal fuel cycle [32].

Motivated by the observations listed above, our present study aims at a better understanding of the fundamental reduction mechanisms by investigating the microstructural evolution of the combusted powder during their reduction process. More specifically, HyDR of combusted iron powder, with and without deep pre-oxidation treatment at 900 °C (for 1 h), is studied by thermogravimetry analysis (TGA) at 400 °C, 450 °C and 500 °C, respectively. Interrupted TGA tests coupled with scanning electron microscopy (SEM), electron backscatter diffraction (EBSD), energy-dispersive X-ray spectroscopy (EDS), *ex-situ* X-ray diffraction (XRD), and together with *in-situ* high-energy X-ray diffraction (HEXRD), were used to investigate the phase distribution and microstructural evolution during the reduction process. The underlying HyDR reaction mechanisms and the effect of a deep pre-oxidation step prior to subsequent HyRD are discussed.

2. Materials and methods

2.1. Materials

Iron oxide powder, named PartOx hereafter, was produced by the combustion of pure iron powder. Details about the combustion process and the characterization of the combusted powder particles were reported in Ref. [36]. The chemical composition of the PartOx sample was measured as Fe-22.4O-0.037Ni-0.035Mn-0.034Mo-0.032Cu-0.015Cr-0.005C-0.001S (in wt. %) using inductively coupled plasma optical emission spectrometry (ICP-OES). The carbon and sulfur content of the combusted particles were measured by the combustion method followed by infrared absorption spectroscopy. The oxygen content was measured by the reduction fusion method, followed by infrared absorption spectroscopy. An additional deep pre-oxidation treatment was applied to the PartOx powder with the aim of fully oxidizing the powder to 100 % hematite. This pre-oxidized powder is referred to as FullOx, hereafter. To produce FullOx powder, PartOx powder was dispersed on a flat alumina holder, heated at 900 °C for 1 h in air, with the holder being shaken every 10 min to minimize sintering. The powders were sieved between 25 μm and 45 μm for the in-situ high energy x-ray diffraction experiment, and over 45 μm for the thermogravimetry experiment. The particle size distribution of PartOx was measured by laser diffraction, using the wet mode with 2 % of tetrasodium pyrophosphate in water as dispersant in the Microtrac Series 5000 SYNC Particle Size Analysis System (see Supplementary Figure S1 for the particle size distributions). The size distribution of FullOx could not be measured but is estimated as similar to PartOx, as it was produced from PartOx and sieved similarly. For the powder sieved over 45 μm (for the thermogravimetry analysis), the mean diameter and standard deviation of the volume distribution were 59.2 μm and 32.2 μm, respectively. The Dv10, Dv50, and Dv90 (indicating the upper size limit containing 10 %, 50 % and 90 % of the volume of the powder) were 15.3 μm, 47.1 μm, and 116.2 μm, respectively.

For the powder sieved between 25 μm and 45 μm (for the high energy x-ray diffraction analysis), the mean diameter and standard deviation of the volume distribution were 32.0 μm and 9.4 μm, respectively. The Dv10, Dv50, and Dv90 (indicating the upper size limit containing 10 %, 50 % and 90 % of the volume of the powder) were 20.1 μm, 30.0 μm, and 45.7 μm, respectively. Pycnometer measurements were applied to measure the density of both PartOx and FullOx powders using AccuPyc II 1340 V3.00 under argon at room temperature, averaged on 5 gas filling cycles and on two samplings.

2.2. Thermogravimetry analysis (TGA)

FullOx and PartOx powder samples were reduced in a TGA setup, with a reactor diameter around 5 cm in diameter [41]. The reduction level X is given as:

$$X(t) = \frac{m_{Fe_2O_3,0} - m(t)}{m_{Fe_2O_3,0} - m_{Fe,f}} \tag{1}$$

where, $m(t)$ is the measured mass at time t, $m_{Fe_2O_3,0}$ is the corresponding mass when iron species are completely oxidized to hematite, and $m_{Fe,f}$ is the corresponding mass when iron species are completely reduced to α-iron. Therefore, PartOx and FullOx begin with an initial reduction level of 0.0567 and 0, respectively, and present a reduction level of 1 when they are fully reduced. For each experiment, about 300 mg of powder was used, which were held in a stainless-steel wire mesh with a mesh size of 500. The samples were exposed to pure hydrogen (99.999 % purity) at a flow rate of 10 L/h during the entire reaction, corresponding to a mean superficial gas velocity of about 1.4 L/m^{2}s. The samples were heated using an infrared furnace (with a reaction chamber of ~0.5 L) at a heating rate of 5 °C/s, then held isothermally at 400 °C, 450 °C, and 500 °C. The target temperatures were reached after 76–96 s, corresponding to a reduction level (X) of less than 0.004, 0.009, 0.02 at 400 °C, 450 °C, and 500 °C, respectively. It should therefore be noted that the reduction happened non-isothermally at the beginning of the process, although more than 98 % of the total conversion occurred isothermally. At the end of the HyDR, the reduced powder was first cooled down to room temperature in hydrogen, then the atmosphere was switched to argon. *In-situ* mass loss of powder was recorded using a thermobalance to evaluate the reduction degree. The powder was also weighed before and after HyDR using a precision scale. Sometimes, a mismatch was observed between the measured mass loss by TGA and the mass change before or after the TGA experiments, due to the fall of particles through the mesh during the setup of the experiments. The conversion curves were therefore based on the measured mass loss recorded by TGA and on the final oxygen content of the reduced powder measured by reduction fusion and infrared absorption spectroscopy.

2.3. Microstructure characterization

Interrupted TGA experiments were conducted to study the microstructural evolution of the powder during the reduction process. However, it should be noted that the reduction levels from the interrupted TGA tests were slightly overestimated (with an increase of the reduction level up to 0.045) as the reduction further proceeded while cooling down the sample from reduction temperature to room temperature in hydrogen. As the relative phase change cannot be decorrelated from the measured reduction level, the *ex-situ* XRD measurements were used here as a reasonable approximation of the phase distribution in the interrupted samples. The phases were identified and their average fractions analyzed using a diffractometer D8 Advance A25-X1. The diffractometer was operated with a cobalt target at 35 kV and 40 mA. The phase distribution was quantified by Rietveld refinement using the software Bruker TOPAS Version 5.0.

The surface regions of the initial and reduced powders (from TGA

experiments, at 500 °C) were measured using the physical adsorption of Kr gas molecules at 77.35 K at the surface of the particles, according to the Brunauer-Emmett-Teller (BET) theory. A BELSORP equipment was used and the measurements were averaged over 3 runs. The microstructure and morphology of the initial and partially reduced powders were probed using scanning electron microscopy (SEM) Zeiss Sigma, equipped with energy-dispersive X-ray spectroscopy (EDS) for local chemical analysis, as well as electron backscattered diffraction (EBSD) for local crystallography analysis. Correlative EDS and EBSD maps were acquired simultaneously using a JEOL-6500F field-emission gun microscope with a voltage of 15 kV and a step size of 50 nm.

2.4. In-situ high-energy X-ray diffraction (HEXRD)

In-situ HEXRD experiments were performed in transmission mode during the ongoing HyDR at the beamline P02.1, PETRA III at DESY [42], to investigate the phase transformation of the individual phases in real-time. The beam energy, the corresponding wavelength, and the beam size of the X-ray were 60 keV, ~0.207 Å, and 1 × 1 mm, respectively. The powders were mounted in an *in-situ* reaction cell [43] equipped with a single-crystal sapphire capillary with an inner diameter of 0.6 mm and a length of 80 mm [43]. The sapphire capillary was heated using a hot air blower attached to the reaction cell externally. The temperature of the samples was calibrated using a thermocouple inserted into the capillary at the sample position before the experiments. A mass of 3.8 mg and 3.4 mg was used for PartOx and FullOx powder, respectively. The samples were heated up in argon at a heating rate of ~18 °C/min to 500 °C. When the target temperature was reached, the gas was switched to pure hydrogen. The flow rate was set to 3 L/h. However, the actual flow was even smaller, as a by-pass flow option was allowed to prevent an increase in the gas pressure due to the obstruction of gas flow by the powders in the capillary (see Supplementary Figure S2 for a schematic of the set-up). The diffraction patterns were recorded every second using an area detector VAREX XRD 4343CT (2880 pixels × 2880 pixels, 150 × 150 μm^2). The sample-to-detector distance was about one meter and in a half-ring configuration. The sample-to-detector distance was precisely determined using a LaB$_6$ standard sample. The two-dimensional diffraction patterns were integrated using the software PyFAI [44]. The phase fraction was analyzed by the Rietveld refinement method using the software MAUD [45].

3. Results

3.1. Microstructure of combusted and deeply pre-oxidized powders

Fig. 1 presents the microstructural analysis of PartOx (Figs. 1b-e) and FullOx (Figs. 1f-i) samples. Fig. 1a shows the XRD profiles for both PartOx and FullOx samples. The phase distribution in PartOx powder was estimated as 51 ± 1 wt. % of magnetite and 49 ± 1 wt. % of hematite by the Rietveld refinement. Full oxidation to 100 % hematite was measured in FullOx powder, both on the XRD profile where only hematite peaks were observed (Fig. 1a) and in EBSD maps where only hematite was locally detected (Fig. 1h).

The surface of PartOx particles revealed linear patterns after combustion. Thin lenticular hematite grains and dendritic magnetite grains of 19 ± 10 μm were observed in the cross-section of the particles (Fig. 1d). During the deep pre-oxidation step, the morphology and internal microstructure of the powder were strongly modified: on the surface, the previous linear surface patterns grew outward to form a network of small hematite grains with a size of 0.45 ± 0.2 μm on the surface (Fig. 1f). Significant grain refinement also occurred inside the particles during the pre-oxidation treatment, resulting in equiaxed hematite grains with an average size of 3 ± 2.9 μm in the FullOx sample, as observed in the cross-section of the particles (Figs. 1g-i).
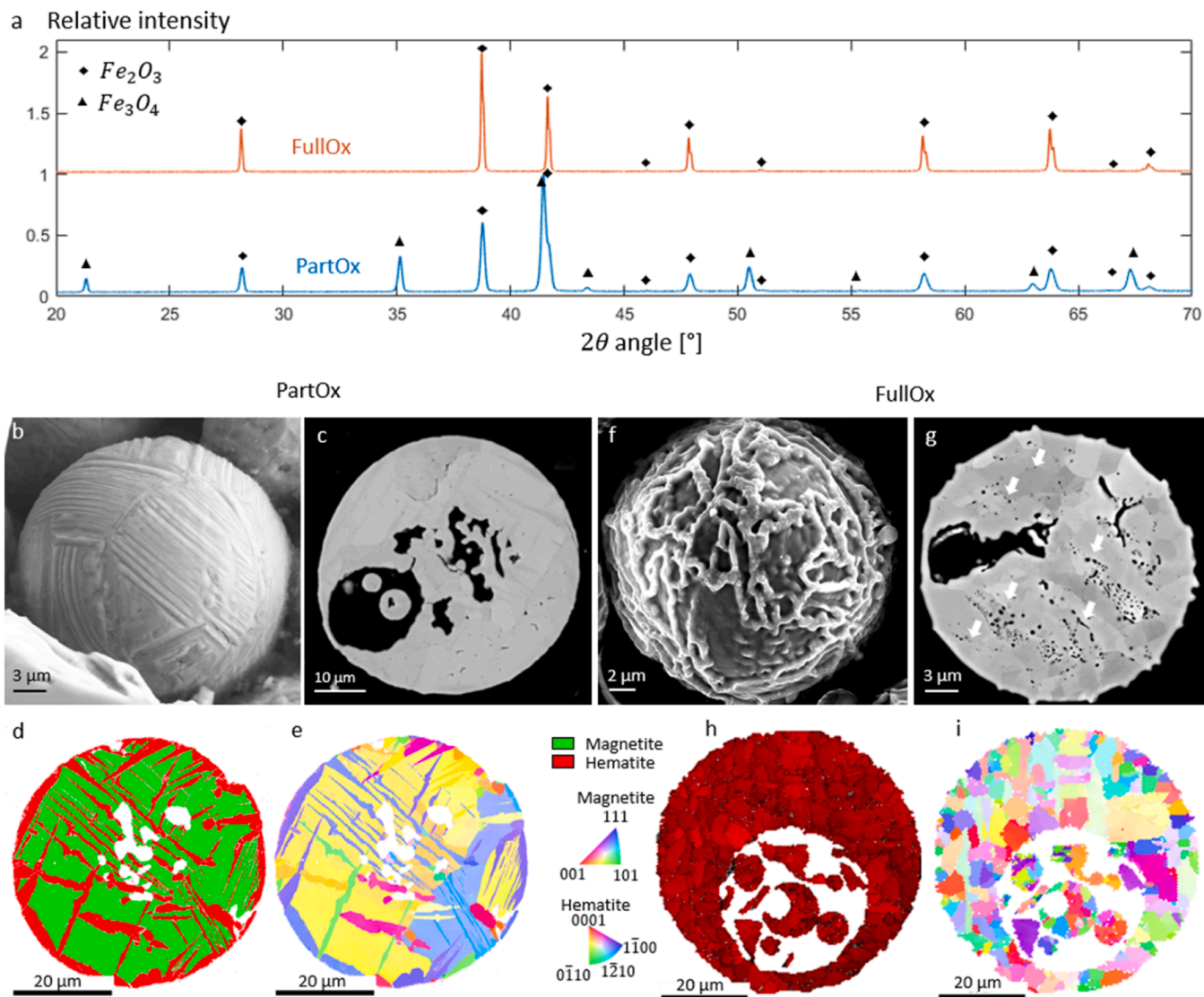
Fig. 1. Microstructural characterization of the combusted iron particles, prior to the reduction process: (a) X-ray diffraction (XRD) analysis (with a Co target); (b-e) combusted powder (PartOx) and (f-i) combusted powder subjected to an additional deep pre-oxidation treatment (FullOx). (b, f) Scanning electron microscopy (SEM) image of the surface, with secondary electrons contrast, and (c, g) of the cross section of a particle, with backscattered electrons contrast. (d, h) Electron backscatter diffraction (EBSD) phase map and (e, i) crystalline orientation map. The arrows in (g) highlight the additional porosities formed during the deep pre-oxidation treatment.

Moreover, the porosity distribution and surface area of the particles were also modified by the deep pre-oxidation treatment. Large porosities were present in PartOx particles (up to 80 % of the particle diameter [36]) and identified as resulting from gas production/entrapment during the combustion process, as documented in our previous study [36]. These large pores were inherited in FullOx particles. In addition, numerous small pore features, in the range of dozens to hundreds of nanometers in diameter, were also formed during the deep pre-oxidation treatment. These newly formed pores were mostly situated at the grain boundaries, as highlighted by white arrows in Fig. 1g. The fraction of non-percolating porosity was investigated in both samples using pycnometer measurements: density values of 5.125 ± 0.003 g/cm^3 and 5.137 ± 0.032 g/cm^3 were measured for PartOx and FullOx, respectively. Based on the theoretical density of dense magnetite (5.18 g/cm^3) and hematite (5.26 g/cm^3) [46] and their respective mass fractions in both samples, the non-percolating porosity was estimated to be 1.8 ± 0.1 vol. % for PartOx particles and 2.3 ± 0.6 vol. % for FullOx particles. A surface area of 0.168 ± 0.077 m^2 g^{-1} and 0.065 ± 0.001 m^2 g^{-1} was measured by BET for PartOx and FullOx particles, respectively.

3.2. Reduction kinetics

Fig. 2 presents the reduction kinetics computed from the measured mass loss in the TGA experiments. The results suggested a strong influence of the reduction temperature on the overall kinetics. An increase in temperature from 400 °C to 450 °C resulted in a decrease in the time required to reach a 95 % reduction by a factor of two, and by a factor of five when increasing the temperature from 400 °C to 500 °C. However, no strong effect of the pre-oxidation treatment was observed on the reduction kinetics; the slight variations between the reduction kinetics of PartOx and FullOx samples were within the experimental scatter when repeating the experiments (see Supplementary Figure S3).

3.3. Phase evolution during reduction at 500 °C

The phase evolution was investigated by *ex-situ* XRD experiments after interrupted TGA and *in-situ* HEXRD during HyDR at 500 °C. The 2D contour map of the X-ray intensity evolution during the *in-situ* HEXRD experiments is shown in Supplementary Figure S4. Fig. 3 presents the
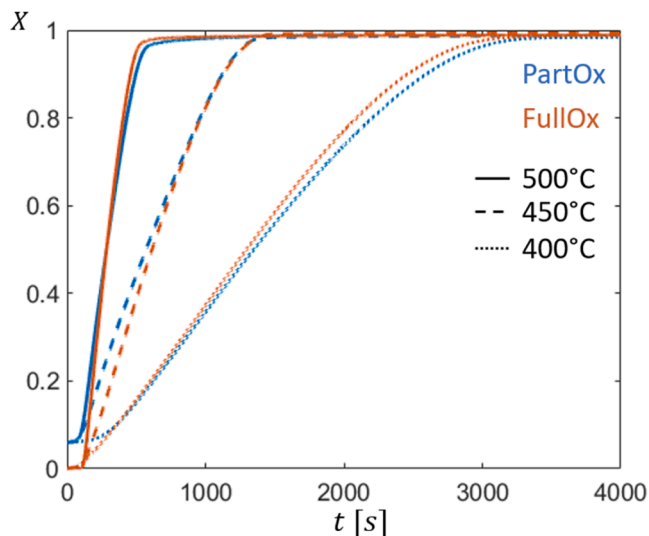
Fig. 2. Reduction kinetics of the combusted powder (PartOx) and the pre-oxidized powder (FullOx) at 400–500 °C, based on the thermogravimetry analysis (TGA).

phase evolution of individual phases, including hematite, magnetite, and α-iron of PartOx and FullOx samples in both TGA and *in-situ* HEXRD experiments. No wüstite formation was observed in any case, as this phase is thermodynamically unstable below 570 °C.

Different types of reduction behavior were observed for both types of samples in the TGA and the *in-situ* HEXRD experiments. A major difference was the sequence of phase transformations. In the *in-situ* HEXRD experiment, the reduction of hematite and magnetite was sequential, *i.e.*, hematite was at first fully reduced to magnetite before the initiation of magnetite reduction to iron. In contrast, all three phases (hematite, magnetite, and α-iron) co-existed in the TGA experiment. As the sample was composed of several particles, it could correspond to a difference in reduction rate in different particles, but it could also be due to the concomitant reduction of both hematite and magnetite in the same particle. This uncertainty was further clarified by the microstructural characterization of the partially reduced particles, as presented in Section 3.4.

In addition, the phase transformation rates of individual phases were significantly larger in the TGA experiment, reaching a full reduction (less than 1 wt. % of remaining iron oxide measured by *ex-situ* XRD) after about 700 s. In contrast, after 1740 s in the *in-situ* HEXRD experiment, 43 wt. % and 75 wt. % of the sample were still composed of magnetite for FullOx and PartOx, respectively. The phase transformation rates of individual phases in both samples were further quantified. In the *in-situ* HEXRD experiments, the transformation rate of hematite was two times larger in the FullOx sample ($12.8 \times 10^{-3} \ s^{-1}$) compared with the PartOx sample ($5.7 \times 10^{-3} \ s^{-1}$). This fact resulted in a complete reduction of hematite at the same time for PartOx and FullOx powders, even though the FullOx sample initially contained twice the amount of hematite as the PartOx sample. The same behavior was observed for the reduction of magnetite into α-iron, with an increase in the α-iron formation rate from $0.2 \times 10^{-3} s^{-1}$ to $0.4 \times 10^{-3} s^{-1}$ with the deep pre-oxidation treatment. Based on the *ex-situ* XRD data from the interrupted TGA experiments, the rate of hematite fraction transformation increased from $2.3 \times 10^{-3} \ s^{-1}$ to $3.8 \times 10^{-3} \ s^{-1}$ after pre-oxidation. The evolution of α-iron behaved non-linearly and was fitted according to the equation $x_{Fe} = 1 - \exp(-k(t - a))$, which represents well the kinetics of a phase transformation governed by the chemical reaction or nucleation and growth. This choice will be discussed in Section 4.2. The kinetic parameter k increased from $7.4 \times 10^{-3} \ s^{-1}$ to $16.7 \times 10^{-3} \ s^{-1}$ with the deep pre-oxidation treatment.

3.4. Microstructural analysis

3.4.1. Cross-section

Figs. 4a-c show the microstructure of PartOx particles partially reduced at 500 °C in the TGA at an average reduction level of 0.08, 0.34, and 0.92, respectively. At the beginning of the reduction process, three different microstructure features were observed in a single particle in SEM images: porous bright grains, dense dark grains, and porous dark grains. The brightness of these grains is given by the intensity of back-scattered electrons, linked in this case mainly to the average atomic weight of the grains, as highlighted by EDS and EBSD in Fig. 5. Figs. 5b and 5c highlight the strong enrichment in iron as well as depletion in oxygen in the grains highlighted as bright in SEM-BSE images, which were identified as α-iron. The surrounding dark grains were identified as either hematite or magnetite using EBSD. Dense magnetite grains corresponded to the initial magnetite grains formed after the combustion process, while porous magnetite grains resulted from oxygen removal during the reduction of the initial hematite grains.

α-Iron grains were initially seen surrounding the holes created by the loss of oxygen during the reduction of hematite in both samples, as shown in Fig. 4a and 4d. Particularly, α-iron preferentially nucleated on porous magnetite rather than on dense magnetite, Fig. 4a. As a consequence, the lenticular hematite grains were preferentially reduced to α-iron before the reduction of the initial dense magnetite grains in PartOx. This gave rise to lines of highly porous α-iron in a matrix of unreduced dense magnetite grains in the middle of the reduction process of PartOx particles (*i.e.*, 0.34 reduction level, as highlighted in Fig. 4b). Fig. 4c presents the cross-section of a fully reduced PartOx particle. Eventually, the porosity was heterogeneous. In the center of the powder, the regions of previous lenticular hematite grains became large and elongated pores, and more porous, while regions of the previous magnetite grains were denser when they were reduced to α-iron.

Fig. 4d, 4e, and 4f present the evolution of the microstructure of FullOx powder for a mean reduction level of 0.07, 0.24, and 1, respectively. A core-shell microstructure was formed at the beginning of the reduction process (Fig. 4d, reduction level of 0.07), *i.e.*, equiaxed hematite grains in the center were surrounded by porous magnetite grains at the surface. α-Iron nuclei were already observed at the very beginning of the reduction process around the pores formed in the reduced hematite, as highlighted by the white arrow in Fig. 4d. Yet, unlike the PartOx sample, α-iron was only observed at the surface of the FullOx particle at the beginning of the reduction, far from the unreduced hematite grains, which subsisted only in the center of the particles. Fig. 4e shows the microstructure obtained after the full reduction of hematite to magnetite, for a mean reduction level of 0.24. Porous magnetite grains formed through the whole cross-section, with α-iron nuclei preferentially formed on the magnetite grain boundaries. Fig. 4f illustrates that a homogeneous porosity distribution was observed in fully reduced FullOx particles.

The role of the initially present pores in the reduction process was also investigated in Fig. 6a, presenting the cross-section of a PartOx particle with a reduction level of 0.32 containing two large cavities.

The first large and spherical cavity is percolating, *i.e.* open to the external atmosphere. Percolating cavities behave like the external surface of the particle, hence presents a layer of reduced iron α-iron on its inner surface of the same thickness as the external surface of the particle. In addition, the other dendritic cavity in Fig. 6a presents almost no ferrite α grain on its inner surface, which consists mostly of magnetite. The absence of ferrite α on its boundaries suggests a more difficult access of the hydrogen gas inside the dendritic cavity. The latter is therefore considered as a "non-percolating" pore in the sense that it displays a slower access to the hydrogen gas, although a 3D characterization would be required to determine its percolation. In the regions between the so-called "percolating" and "non-percolating" pores (region I in Fig. 6a), several α-iron grains were still observed due to the proximity of this region to the open surface. The inset in Fig. 6a highlights an interesting
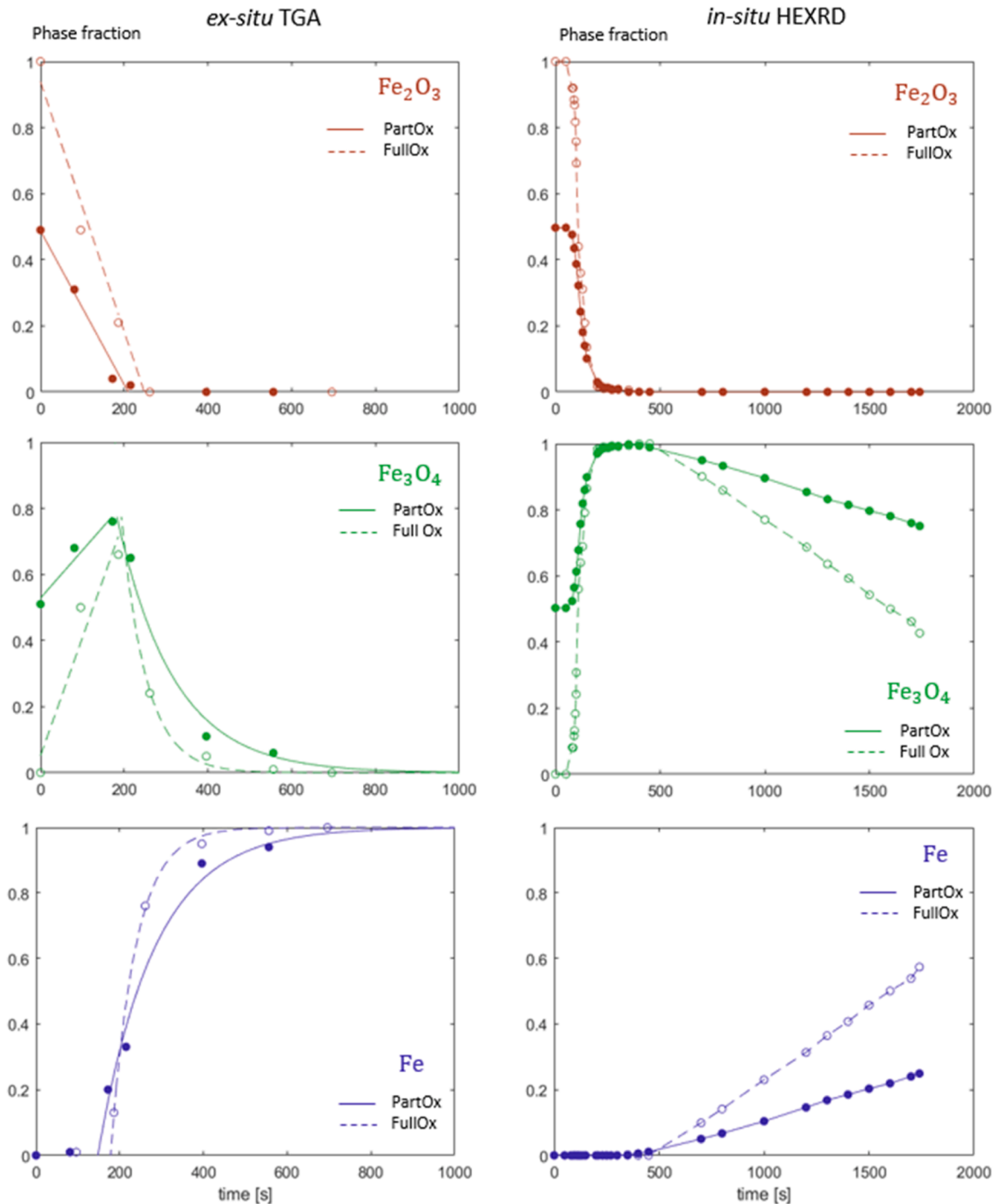
Fig. 3. Phase evolution of individual phases in PartOx and FullOx samples during hydrogen-based direct reduction at 500 °C, investigated by ex-situ X-ray diffraction (XRD) at various reduction levels in interrupted thermogravimetry analysis (TGA) experiments, and by in-situ high-energy X-ray diffraction (HEXRD).

phenomenon: several α-iron grains were observed to preferentially nucleate in the reduced magnetite situated across the non-percolating cavity, in front of the region close to the percolating cavity (region II in Fig. 6a). Such observations suggest that after reducing the iron oxides around the external surface and around the percolating cavities, the access of hydrogen inside a non-percolating cavity facilitates its diffusion inside the particle. The presence of non-percolating pores can therefore be beneficial in the beginning of the reduction process for the reductant gas to access the center of the particles through them.

Fig. 6b presents the cross-section of a PartOx particle with a reduction level of 0.92, *i.e.,* at the end of the reduction process. In this particle,

only a few islands of dense magnetite remained among the α-iron microstructure. In particular, most remaining magnetite grains were located close to small cavities, as highlighted by arrows in Fig. 6b. This finding suggests that the oxidized magnetite was stabilized by the presence of these cavities, probably non-percolating as discussed in Sector 4.3.

3.4.2. Surface analysis

Fig. 7 presents the evolution of the surface morphology of the powders at 500 °C in the TGA experiments. The number and size of pores increased with reduction time due to the progressive removal of oxygen.
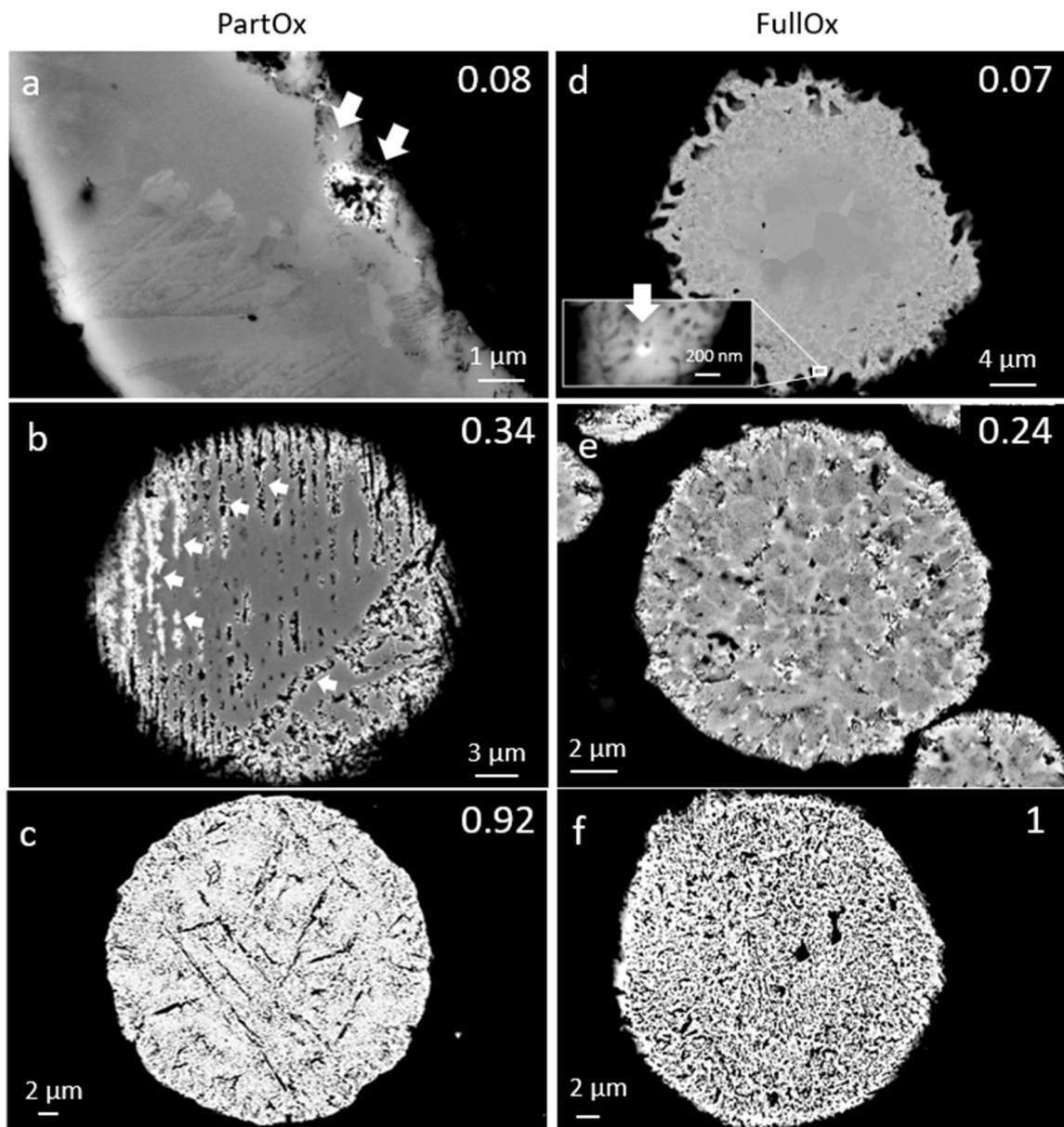
Fig. 4. Scanning electron microscopy (SEM) images with backscattered electrons detector presenting the cross-section of partially reduced particles of (a-c) PartOx and (d-f) FullOx powders during their reduction at 500 °C in the thermogravimetry (TG) reactor, with their average reduction level estimated from XRD measurements given in the top right corner. The white arrows highlight the presence of porous α-iron grains.

The localization of the reduction in the lenticular hematite grains in the PartOx sample (highlighted in Fig. 4a-c) was also observed in Fig. 7a-c, forming lines of coalesced pores on the surface of the reduced PartOx particles. Fig. 7d-f illustrates the more homogeneous porosity distribution in the reduced FullOx particles.

The surface area of the powders fully reduced at 500 °C was measured by BET, showing a decrease in the final surface area by applying a deep pre-oxidation treatment before the actual reduction process (1.280 ± 0.039 m^2 g^{-1} for FullOx particles and 1.734 ± 0.042 m^2 g^{-1} for PartOx particles).

Fig. 8 presents the surface morphology of fully reduced PartOx and FullOx powders at 400 °C, 450 °C, and 500 °C, respectively. Linear features of pores were observed on the surface of PartOx particles at all reducing temperatures, while the pores of FullOx particles were more homogeneously distributed. As reported in the literature [31], the size of the pores increases with the reaction temperature. An interesting observation of FullOx particles was the formation of many agglomerates

at the end of the reduction; namely, smaller particles were sintered with the larger particles and attached to their surfaces. This phenomenon was rarely observed in reduced PartOx particles.

4. Discussion

4.1. Influence of deep pre-oxidation

The topography of the external surface of the combusted particles was modified during the deep pre-oxidation treatment. Our previous study suggested tha the solid-state oxidation of magnetite to hematite during the cooling of the combusted particles resulted in linear patterns on the surface of PartOx particles [36]. Similar patterns were previously reported in the literature, which were rationalized by the oxidation of magnetite to hematite [47] and the associated outgrowth of hematite along preferred orientations [48]. During oxidation, outward iron cation diffusion is indeed favored compared with inward oxygen anion
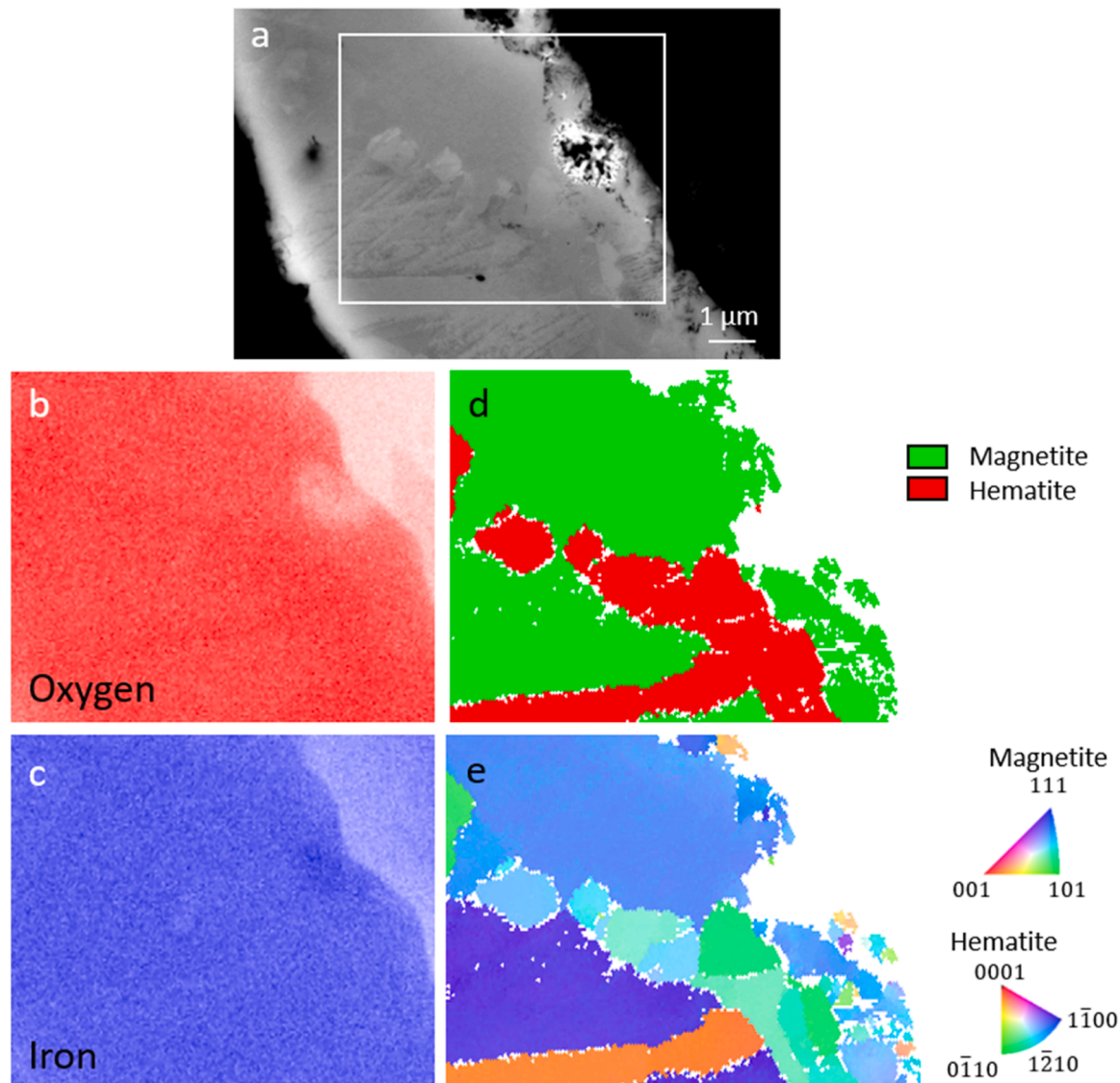
Fig. 5. Electron backscatter diffraction (EBSD) and energy dispersive spectroscopy (EDS) maps of a PartOx particle partially reduced to a reduction level of 0.03 in the thermogravimetry (TG) reactor at 500 °C. (a) The corresponding scanning electron microscopy (SEM) image, (b) oxygen and (c) iron EDS map, (d) EBSD phase map, and (e) EBSD inverse pole figure (IPF) related to the sample normal direction.

diffusion in the magnetite crystal structure [49]. With further deep pre-oxidation, magnetite was fully oxidized to hematite and the thickness of the surface linear patterns increased (Fig. 7). The branches of this network were no longer parallel to one another, showing material diffusion in addition to the growth of hematite. The formation of equiaxed grains (Fig. 1h) is mainly due to a grain refinement phenomenon during the oxidation from magnetite to hematite, *i.e.*, several hematite grains nucleated from one magnetite grain. Monsen [37] observed such phenomenon and reported an increase in the proportion of equiaxed grains compared with lenticular-shaped grains when increasing the oxidation temperature of magnetite. Moreover, the size of the equiaxed hematite grains also increased with the oxidation temperature [37]. Larger equiaxed grains are preferred at higher oxidation temperatures due to the improved ionic diffusion, which allows the system to decrease its total interface energy. The decrease in surface area during the oxidation process was also previously reported in the literature during oxidation at 1100 °C [48]. It was attributed to an activated sintering process at high temperatures, to decrease the internal energy of the system. In this case, the surface area could also be further reduced during the pre-oxidation process due to the closing of fine cracks and of

some initially percolating porosities, present in the combusted iron particles [36].

Preferred agglomeration and local sintering of smaller particles on bigger particles were highlighted in FullOx particles in Fig. 8d, e, and f. Such favored sticking is a sign that deep pre-oxidation could accelerate defluidization in fluidized bed reactors [50]. In contrast, Zheng et al. [19] observed that defluidization was postponed to larger reduction levels by prior oxidation of a magnetite-based ore. This beneficial effect was due to an increase in porosity with prior oxidation of the dense magnetite ore, which resulted in a decrease in the fresh iron formed on the surface of the particles. An increase in non-percolating porosities was measured after the deep pre-oxidation process, due to the favored outward diffusion of iron cations [49]. Yet, the non-percolating porosities created by the deep pre-oxidation treatment (~0.2 %) are less significant compared with the non-percolating porosities created during the combustion process (~1.8 %). In the case of the combusted powder, the increase in porosity during deep pre-oxidation is negligible compared with the strong increase in its surface roughness due to the formation of a thick oxide network at its surface. Therefore, the deep pre-oxidation treatment favored the sticking behavior during the HyDR
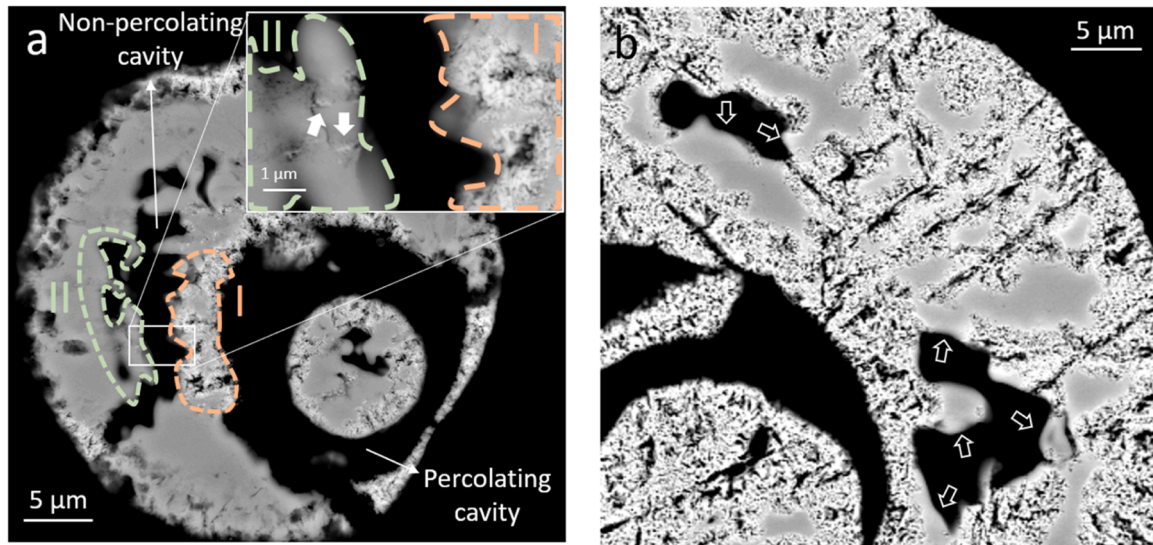
Fig. 6. Influence of the porosities on the reduction process. Scanning electron microscopy (SEM) images with backscattered electrons contrast of the cross-section of PartOx particles, partially reduced in the thermogravimetry (TG) reactor at 500 °C at a reduction level of (a) 0.32 and (b) 0.92. The white arrows highlight the presence of α-iron in the inset of (a) and of remaining magnetite near the porosities in (b).

of combusted particles. However, the effect of prior oxidation on the defluidization behavior should be investigated in more detail in a fluidized bed reactor.

4.2. Reduction kinetics

The reduction of hematite at the temperatures considered here (400–500 °C) is divided into two steps, each being represented by its conversion parameter X_1 and X_2:

$$X_1 : Fe_2O_3 + H_2 \rightarrow Fe_3O_4 + H_2O \tag{2}$$

$$X_2 : Fe_3O_4 + 4H_2 \rightarrow 3Fe + 4H_2O \tag{3}$$

Different methods exist to analyze the reduction kinetics of a material based on its conversion evolution. In this work, a model-fitting method was chosen with the aim of better comprehending the fundamental physical mechanisms behind the reduction process. The different individual reactions can all be approximated in the general form:

$$\frac{dX}{dt} = f(X)k(T), \tag{4}$$

where $f(X)$ is the physics-based model to be fitted, and the temperature dependence $k(T)$ is given by an Arrhénius law:

$$k(T) = A\exp\left(-\frac{E_a}{RT}\right), \tag{5}$$

Where E_a is the activation energy [kJ. mol^{-1}]. The model can also be expressed as $g(X)$ evolving linearly with time:

$$g(X) = \int \frac{1}{f(X)} dX = kt \tag{6}$$

Table 1 lists the main models considered for the reduction of iron oxide [51,52]:

(i) Phase boundary, core-shell, or contracting sphere model, where the kinetics is limited by the reduction reaction at the boundary between the reacting phase (in the core of a spherical particle) and the product phase (in the shell of a spherical particle). In this model, the reaction boundary moves inward from the surface towards the center of the particle.

(ii) Nucleation and growth, or Avrami-Erofeev model, where the kinetics is limited by the nucleation of the product phase and its growth from the reaction phase. This model has an additional parameter n (varying between 2 and 4) which depends on the nucleation process as well as on the dimension of the growth.

(iii) Gas film resistance, where the kinetics is limited by the external mass transport through the gas film surrounding the particle surface.

(iv) Three-dimensional solid-state diffusion, where the kinetics is limited by the diffusion of the reactants/products through the reduced solid layer.

A strong difference in reduction kinetics was observed between the TGA and *in-situ* HEXRD experiments (Fig. 3), showing that the reduction reaction was limited by the experimental conditions in one of the set-ups. During *in-situ* HEXRD experiments, the two reduction steps were observed to proceed in a successive manner, with the full conversion of hematite into magnetite before the subsequent reduction of magnetite into α-iron. The conversion rates of hematite X_1 and magnetite X_2 are hence given by the decay rates of hematite and magnetite, respectively, as given in Section 3.3. Both conversions evolve linearly with time, which could correspond to the kinetics of a gas film resistance-limited reaction (Table 1). The reduction model $f(X)$ depends on the driving force for external mass transport, *i.e.*, the hydrogen concentration gradient between the surface of the particle and the external boundary of the gas film [51]. Considering the reduction reaction at the surface of the particle and the gas diffusion to the gas film to be much faster than the mass diffusion through the gas film, the concentration gradient through the gas film is relatively constant. Therefore, the reduction level evolves linearly with time [51]. Such gas film resistance-limited reaction is generally obtained when the superficial gas velocity at the surface of the particles is too low. The gas flux was, however, set to obtain a large average superficial gas velocity (2900 L/m^{2}s). Most probably, the gas did not pass through the particles. As the set-up was designed with a by-pass flow to avoid any overpressure phenomenon in the capillary, the actual local superficial gas velocity inside the capillary is unknown. The latter is probably too small and at the origin of a gas film resistance-limited reaction. A strong influence of pre-oxidation on reaction kinetics was observed, increasing the reaction constant by a factor of 2 for both hematite and magnetite reduction in FullOx compared with PartOx powder. In a gas film diffusion-limited reaction, the reaction
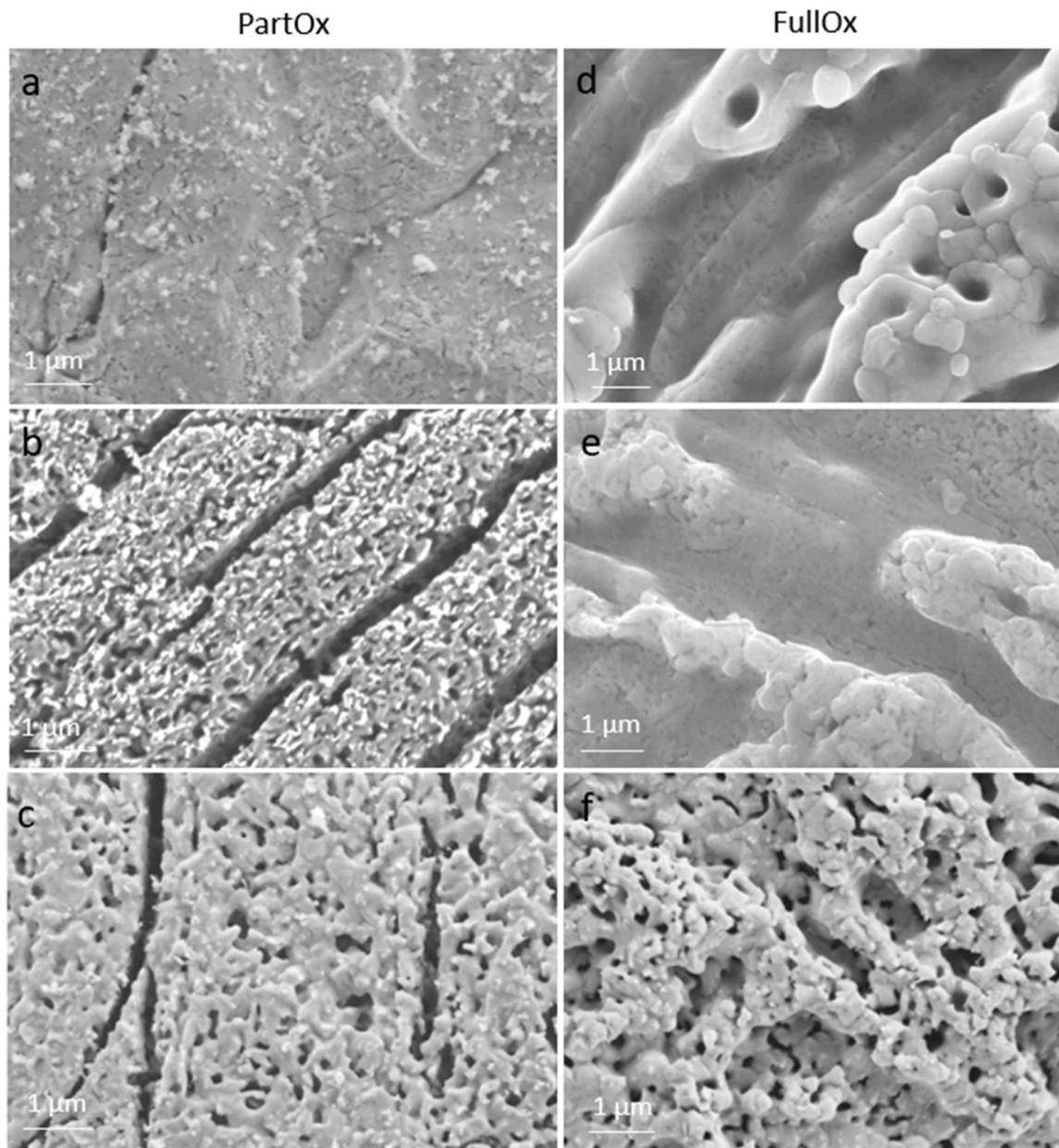
Fig. 7. Scanning electron microscopy (SEM) images with secondary electrons contrast of the evolution of the surface morphology of (a-c) PartOx and (d-f) FullOx powders during their reduction at 500 °C in the thermogravimetry (TG) reactor, for a reduction level of (a) 0.08, (b) 0.34, (c) 0.92, (d) 0.07, (e) 0.24, and (f) 1.

kinetics are governed by (i) the concentration gradient through the gas film, (ii) the mass transfer coefficient through the gas film and (iii) the surface area of the particles [51]. The concentration gradient through the gas film (i) is considered constant and similar for both PartOx and FullOx, given by the thermodynamic stability of product phase for the gas concentration near the particle surface and by the gas concentration at the surface of the gas film, close to the concentration of the input gas flow. The delay observed between the end of hematite reduction and the beginning of magnetite reduction could be explained by the modification of the local hydrogen/water concentration at the particle surface. A sufficient hydrogen/(hydrogen+water) ratio (>82 vol % at 500 °C) is required as a thermodynamical condition to allow reduction of magnetite to iron. Furthermore, the mass transfer coefficient through the gas film (ii) can be strongly influenced by the superficial gas velocity. Although the same gas flux was used in both experiments, the separation of the gas between the capillary and the by-pass could induce a different local superficial gas velocity around the powders. Finally, a larger

reduction rate could also be explained by a larger surface area of the reacting particles (iii). FullOx powder presents an initial mass of hematite, hence a reactive surface area, twice as large as PartOx powder [51]. Moreover, the reduction of hematite creates micropores in the powder through the removal of oxygen, also increasing its reactive surface area for the following reduction of magnetite. Therefore, the reaction rate of iron oxide reduction in the case of a gas diffusion-limited reduction process can be expected to be proportional to the initial hematite content. An initial deep pre-oxidation step would be particularly interesting for achieving faster reduction kinetics under conditions where the hydrogen flux is limited.

In the TGA experiment, the hydrogen flux was set large enough (10 L/h) to obtain a reduction process that is not limited by the external diffusion of hydrogen. Contrary to what was observed in the HEXRD experiment, the reduction of hematite and magnetite was not successive but partially concomitant. Thus, the kinetics of individual reaction steps need to be decorrelated to use the model-fitting method. Two conversion
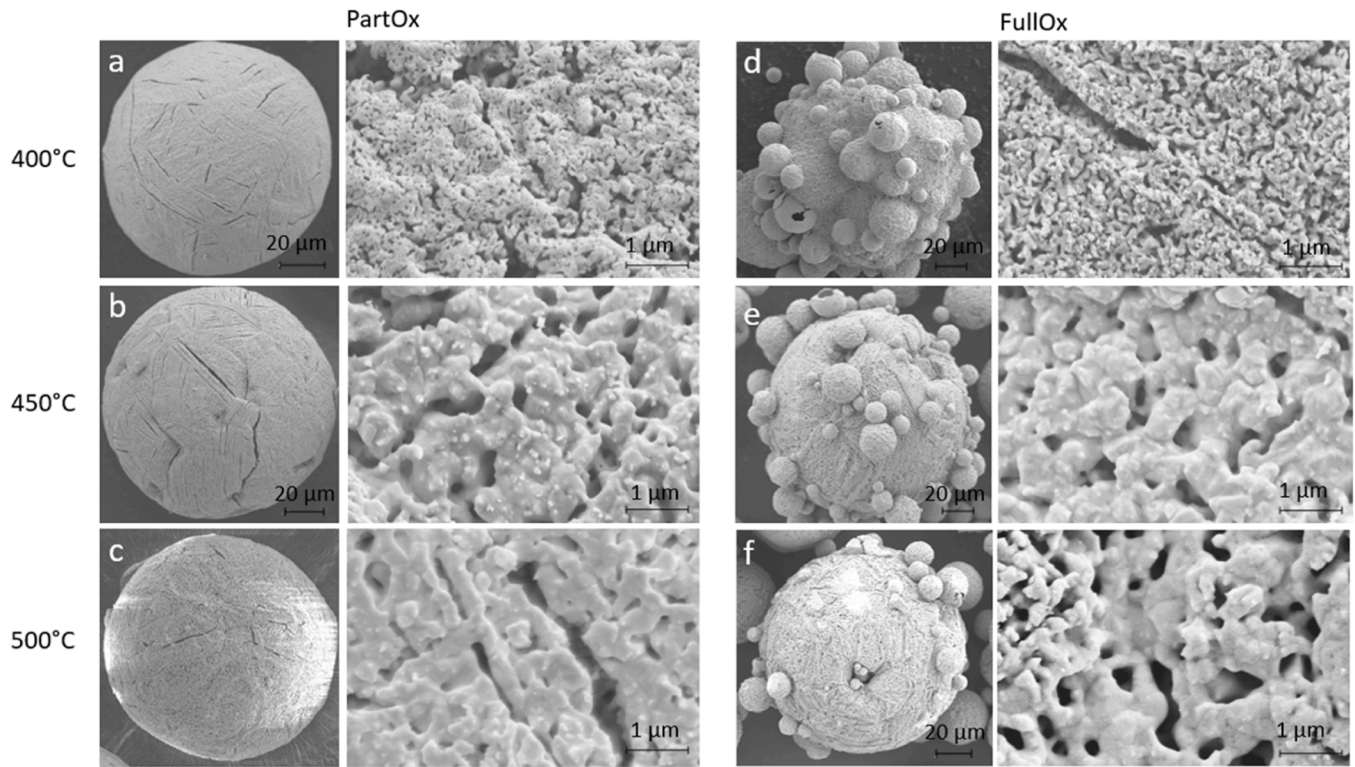
Fig. 8. Scanning electron microscopy (SEM) images with secondary electrons contrast of the surface porosity formed after full reduction of (a-c) PartOx powder and (d-f) FullOx powder at (a, d) 400 °C, (b, e) 450 °C and (c, f) 500 °C in the thermogravimetry (TG) reactor.

Table 1
Model description of the conversion X for various dominant mechanisms of the reduction process [51,52].

Model	Abbreviation	g(X)
Phase boundary	PB	$1 - (1 - X)^{1/3}$
Nucleation and growth	NG	$(-\ln(1 - X))^{1/n}$
Gas film resistance	GF	X
Solid diffusion	SD	$1 - 3(1 - X)^{2/3} + 2(1 - X)$

parameters are defined for each reduction step: X_1 for the reduction of hematite to magnetite and X_2 for the reduction of magnetite to α-iron. Following Hessels et al. [31], the mass evolution of the different phases varies with the conversions X_1 and X_2:

$$m_{\text{Fe}_2\text{O}_3} = m_{\text{Fe}_2\text{O}_3,0} \left(1 - X_1\right) \tag{7}$$

$$m_{\text{Fe}_3\text{O}_4} = m_{\text{Fe}_2\text{O}_3,0} \left(\frac{2 M_{\text{Fe}_3\text{O}_4}}{3 M_{\text{Fe}_2\text{O}_3}} X_1\right)(1 - X_2) \tag{8}$$

$$m_{\text{Fe}} = m_{\text{Fe}_2\text{O}_3,0} \left(\frac{2M_{\text{Fe}}}{M_{\text{Fe}_2\text{O}_3}} X_1\right) X_2 \tag{9}$$

where m_i and M_i corresponds to the powder mass and molar mass of each phase i, respectively. $m_{\text{Fe}_2\text{O}_3,0}$ is the mass of the initial powder if fully oxidized to hematite. The total conversion of the reduction is given by:

$$X = \frac{m_{\text{Fe}_2\text{O}_3,0} - \left(m_{\text{Fe}_2\text{O}_3} + m_{\text{Fe}_3\text{O}_4} + m_{\text{Fe}}\right)}{m_{\text{Fe}_2\text{O}_3,0} - m_{\text{Fe},f}} \tag{10}$$

where $m_{\text{Fe},f}$ corresponds to the mass of the final powder when fully reduced to iron. Implementing Eqs. (7)–(9) in Eq. (10), the total conversion can be expressed by the conversion of each reaction X_1 and X_2:

$$X = \frac{X_1 \left(1 - \frac{2}{3}\frac{M_{\text{Fe}_3\text{O}_4}}{M_{\text{Fe}_2\text{O}_3}}\right) + X_1 X_2 \left(\frac{2}{3}\frac{M_{\text{Fe}_3\text{O}_4}}{M_{\text{Fe}_2\text{O}_3}} - \frac{2M_{\text{Fe}}}{M_{\text{Fe}_2\text{O}_3}}\right)}{1 - \frac{2M_{\text{Fe}}}{M_{\text{Fe}_2\text{O}_3}}} \tag{11}$$

The total conversion expressed in Eq. (11) was fitted on the experimental conversion curves (given in Fig. 2), using the models summarized in Table 1 to express X_1 and X_2. A gas diffusion limited reaction was eliminated in this case by increasing the flow rate until the reduction kinetics were independent on the applied flow rate. X_1 and X_2 were modeled as either a phase boundary (PB), nucleation and growth (NG) or solid-state diffusion (SD) limited reaction step. Therefore, 9 different model combinations were used to express the total conversion X. Table 2 presents the goodness of fit, determined by the R-square of the fit, for each model combination, for PartOx and FullOx at different temperature. The graphical representation of the best fits is given in Fig. 9. The graphical representation of the fit obtained for each model combination at 500 °C for FullOx and PartOx is given in Supplementary Figures S5 and S6.

A valid concern associated with such forward model-fitting methods is that several model combinations can present a similarly good fit, as shown in Fig. 9 and Table 2. This means that such a method alone is not sufficient to unambiguously identify the dominant mechanisms governing the reduction process. Yet, additional indicative insights can be obtained in association with the microstructural analysis of the powder in its partially reduced state (Fig. 4).

For FullOx powder, the microstructural analysis shows a clear core-shell structure at the beginning of the reduction process with the remaining hematite grains in the center and the reduced magnetite slowly growing from the surface to the core. This phenomenon is typical of a phase boundary-dominant reduction. α-Iron nucleates first around the pores created by the reduction of hematite to magnetite at the beginning of the reduction process. Then, α-iron grains nucleate and grow preferentially at the grain boundaries of the reduced magnetite. It corresponds well to the results of the model-fitting method, supporting a

Table 2

The goodness of fit, quantified in terms of the R-square values of the fits, for the multi-model fit of the total conversion X using Eq. (11) and the different models (listed in Table 1) to represent the conversion of X_1 *and* X_2. The obtained best fit is highlighted in bold.

| R-square n	PB+PB	PB+NG	PB+SD	NG+PB	NG+NG	NG+SD	SD+PB	SD+NG	SD+SD
400 °C PartOx	0.9966	0.9969	0.9823	0.9931	**0.9982**	0.9522	0.9969	0.9943	0.9752
450 °C PartOx	0.9933	0.9926	0.9815	0.9906	0.9956	0.9422	**0.9962**	0.9902	0.9747
500 °C PartOx	0.9974	**0.9982**	0.9850	0.9935	0.9978	0.9536	0.9974	**0.9982**	0.9771
400 °C FullOx	0.9952	**0.9993**	0.9717	0.9941	0.9972	0.9601	0.9954	0.9976	0.9787
450 °C FullOx	0.9965	**0.9992**	0.9753	0.9952	0.9982	0.9632	0.9982	0.9983	0.9819
500 °C FullOx	0.9935	**0.9988**	0.9775	0.9950	0.9978	0.9605	0.9938	0.9950	0.9773
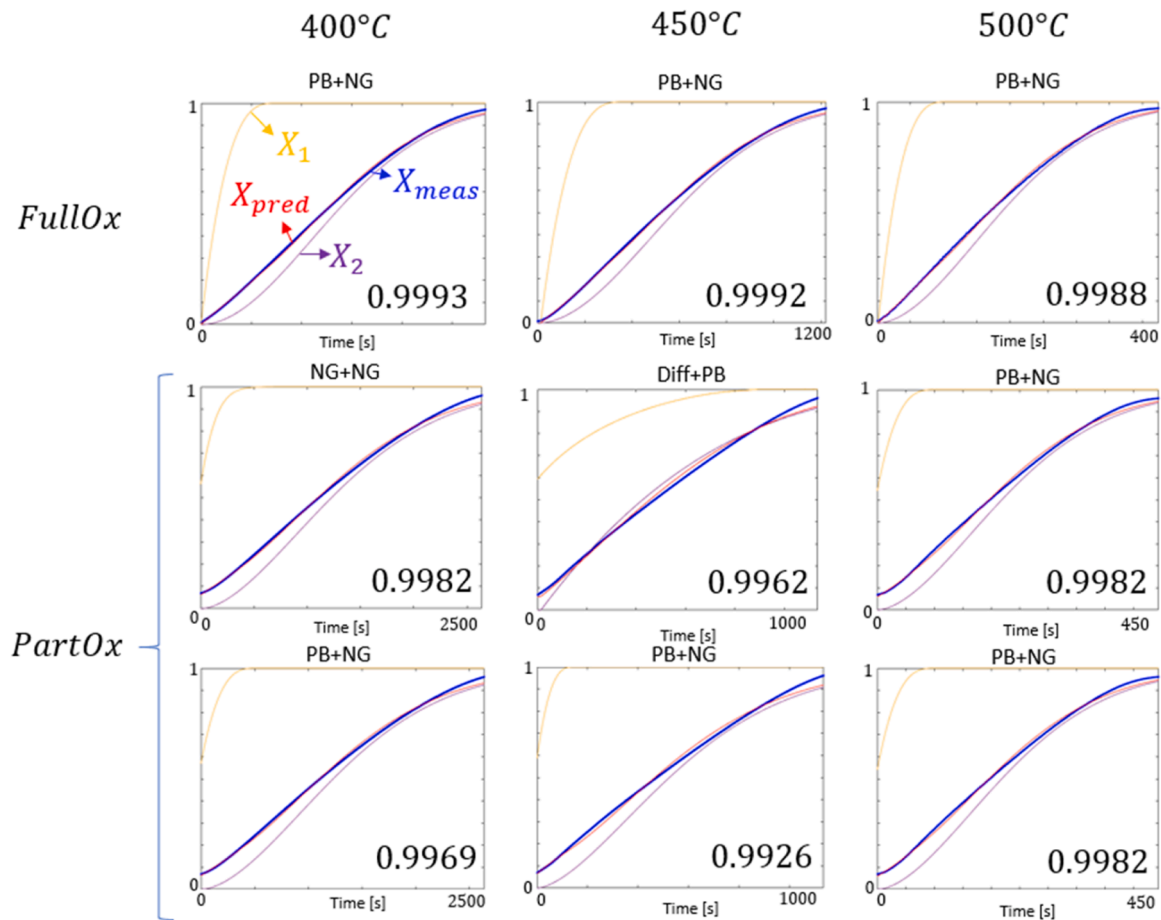
Fig. 9. Multi-model fitting the total conversion X using Eq. (11) and the models listed in Table 1 for X_1 and X_2. The graphics presenting the best goodness of fit, given in the bottom-right corners, are presented. The abbreviations PB, NG and SD correspond to a phase boundary, nucleation and growth, and 3D solid diffusion model, given as the models representing X_1 and X_2, respectively. The multi-models considering a phase boundary for X_1 and a nucleation and growth model for X_2 for PartOx are also given for all temperatures, for sake of comparison.

scenario where a phase boundary model prevails for the reduction of hematite and a nucleation and growth model for the reduction of magnetite, respectively. The fitted kinetic constant k for the reduction of hematite to magnetite increases with temperature from $1.3 \times 10^{-3}\ s^{-1}$, $2.8 \times 10^{-3}\ s^{-1}$ to $9.8 \times 10^{-3}\ s^{-1}$ at 400 °C, 450 °C and 500 °C, respectively. It corresponds to a preexponential factor of $4.9 \times 10^3\ s^{-1}$ and an apparent activation energy of 85.2 kJ. mol^{-1} (see Arrhenius plot in Supplementary Figure S7). It should be noted that these kinetic

constants should be considered carefully as the beginning of the reduction occurred non-isothermally. A stronger increase in the fitted kinetic constant k is obtained for the reduction of magnetite, from $0.6 \times 10^{-6}\ s^{-1}$, $3.7 \times 10^{-6}\ s^{-1}$ to $49.3 \times 10^{-6}\ s^{-1}$ at 400 °C, 450 °C and 500 °C, respectively. It corresponds to a preexponential factor of $1.5 \times 10^8\ s^{-1}$ and an apparent activation energy of 186.0 kJ. mol^{-1} (see Arrhenius plot in Supplementary Figure S7). The fitted parameter n describing the nucleation and growth dimension is similar at the different temperatures (1.9 at 400 °C and 450 °C and 1.8 at 500 °C),

showing that a nucleation and growth model described well the reduction of magnetite in FullOx powder at low temperature.

For PartOx powder, the dominant mechanisms are less obvious. The best goodness of fit predicts a different model combination for each temperature. However, the shape of the fitted X_1 curves at 450 °C and 500 °C is physically unlikely, with an initial hematite content larger than 0.5 and a very slow hematite reduction rate, predicting the remaining presence of hematite for a reduction level of more than 0.7. In comparison, the model combining a phase boundary-governed hematite reduction and a nucleation and growth-limited magnetite reduction is physically more likely, although they present a lower goodness of fit as compared with the models fitted on FullOx curves. Regarding the microstructural analysis, the reduction of hematite starts from the external surface (or from the surface of the percolating cavities) and grows toward the center of the particles, similar to what is observed for the FullOx case. However, the derivation of the phase boundary model is based on the hypothesis of a contracting sphere [53], which does not correspond to the complex geometry of the lenticular-shaped hematite grain boundaries. This could explain the difficulty to model correctly X_1. Regarding the reduction of magnetite, the latter can be divided into two categories. First, the porous magnetite formed from the initial hematite grains is reduced to α-iron, following the same process as in the FullOx case, *i.e.* a nucleation and growth mechanism. Then, the initial dense magnetite is reduced by the propagation of the α-iron/magnetite boundary towards the center of the dense magnetite, as illustrated by the porosity gradient in Fig. 4c. Similar to the reduction of hematite, it corresponds to a phase boundary model. However, the expression derived for g(x) in Table 1 for a phase boundary model corresponds to a spherical particle. In this case, the phase boundary is defined by the boundaries of the multiple lenticular-shaped hematite grains, which is too complex to analytically derive from simple first-order rate equations. In the case of PartOx, the classically used models do not well represent the reduction mechanisms governed by both a nucleation and growth of α-iron in reduced magnetite and a phase boundary propagation with a complex boundary geometry. These microstructural observations can explain why the goodness of the multi-model fit is not as good for the PartOx sample compared with the FullOx sample. A more detailed model, such as phase-field modeling, could be used as an alternative to correctly represent the reduction process of combusted iron powder [54].

4.3. Influence of the microstructure on the reduction process

Strong localization of the reduction process is observed at the location of the lenticular hematite grains, as shown by the formation of elongated pores at the surface and inside the cross-section of reduced PartOx particles. This phenomenon is expected from the faster diffusion of hydrogen through the porosity network formed during hematite to magnetite reduction. Comparatively, a deep pre-oxidation treatment to fully oxidize the powder to hematite homogenizes the reduction process, resulting in a much more homogeneous distribution of porosities at the end of the reduction process.

A larger surface area could be expected after the full reduction of the deeply oxidized FullOx powder compared to the fully reduced combusted PartOx powder, because the initially larger oxidation level of FullOx particles is associated with a larger oxygen removal during the reduction process. Nevertheless, a lower surface area is measured in the reduced FullOx powder (1.280 ± 0.039 m^2 g^{-1} for FullOx particles and 1.734 ± 0.042 m^2 g^{-1} for PartOx particles). This difference could be due to an inherited smaller initial surface area in FullOx particles (0.065 ± 0.001 m^2 g^{-1}) compared to PartOx particles (0.168 ± 0.077 m^2 g^{-1}), but the difference in surface area in the initial particles (0.1 m^2 g^{-1}) is lower than the difference obtained after reduction (0.45 m^2 g^{-1}), suggesting that the final difference in surface area is only minorly affected by the initial surface area, but rather comes from the reduction process itself. The difference in surface area could come from the

different pore size distribution in the two reduced powders: for the same volume of pores, a smaller pore size will strongly increase the associated surface area. Compared with reduced FullOx particles, PartOx particles present a few large and elongated pores but also a large number of smaller pores formed from the reduction of the dense initial magnetite grains. These smaller pores could be at the origin of the relatively larger pore size in PartOx particles. However, experimental variations such as a difference in sampling (a sampling of only 0.03 g could be recovered for the BET measurement out of the reduced powder of 0.2 g after the different experimental characterization) cannot be ruled out.

Another important observation is the nucleation of α-iron at the very beginning of the reduction process, illustrating a relatively low activation energy for α-iron nucleation. Yet, the co-presence of hematite and α-iron was not observed in the *in-situ* HEXRD experiments. It can be concluded that the fast nucleation of α-iron during the TGA is due to a kinetic effect. When the reduction process is slower, limited by the hydrogen diffusion at the surface of the particle in the case of the HEXRD experiments, the diffusion of reactants and products inside the particles is fast enough to allow a full reduction of hematite to magnetite before the nucleation and growth of α-iron.

The number of nucleation sites for α-iron, *e.g.*, grain boundaries, could be increased by microstructure refinement, increasing their density. This is especially interesting for the reduction of particles with a large hematite content, where the reduction of porous magnetite is dominated by the nucleation and growth of α-iron. Decreasing the temperature of the deep pre-oxidation treatment is expected to form finer hematite grains and potentially increase the surface area of the particles [22], therefore improving the reducibility of the deeply oxidized combusted particles.

Regarding the presence of cavities, percolating cavities are favorable for the reduction process by decreasing the relative solid-state diffusion distances, but the role of non-percolating cavities is less straightforward. Non-percolating cavities can be expected to facilitate the reduction process in the beginning by providing free surfaces for chemical reactions and accelerating the diffusion of the reactants by gas diffusion through the cavity, thus reducing the relative diffusion distances. However, magnetite was also observed to be stabilized around cavities at the end of the reduction process (Fig. 6b). This phenomenon could be explained by the accumulation of water in non-percolating cavities, thermodynamically stabilizing the oxidized phase over iron. The trapped water can even lead to re-oxidation of the previously reduced iron around isolated pores, a phenomenon that was investigated at a microscopic scale by Zhou et al. [28] during the hydrogen-based direct reduction of wüstite. The reduction process around non-percolating cavities during the HyDR process should therefore be further investigated for the current scenario of powder reduction in more detail to better understand its role throughout the whole reduction process.

5. Conclusions

In the present study, the influence of deep pre-oxidation on the hydrogen-based direct reduction of combusted iron powder at 400–500 °C was investigated using *in-situ* high-energy X-ray diffraction (HEXRD), thermogravimetry analysis (TGA), and microstructural analysis of the partially and completely reduced powders.

In the *in-situ* HEXRD experiments, the local superficial gas velocity of hydrogen around the particles was limited by the experimental set-up and thus reduction kinetics were limited by the diffusion of hydrogen through the gas film around the particles. In the TGA experiment, a multi-model fitting analysis was applied to investigate the dominant mechanisms of the reduction process, together with a microstructural analysis of the partially reduced powders. In deeply pre-oxidized powder (FullOx), the reduction of hematite is dominated by a phase boundary model or core-shell model. The further reduction of magnetite is limited by the nucleation and growth of α-iron grains, which form preferentially around the pores formed during the reduction of hematite

and at the grain boundaries of the reduced magnetite. In the combusted powder (PartOx), the reduction of the initial hematite grains to α-iron follows the same mechanisms as in the deeply oxidized powder. However, its kinetics are not well represented by the classical core-shell model due to the more complex microstructure, particularly due to the lenticular-shaped hematite in the magnetite matrix. Moreover, the reduction behavior of magnetite is distinguished by a nucleation and growth of α-iron mechanism for the porous magnetite (formed by reducing hematite) and by a phase boundary mechanism for the initially dense magnetite grains.

An increase in the reduction rates was observed for both hematite and magnetite reductions in the deep pre-oxidized sample. When the reaction is limited by the resistance of the gas film around the particles, both reduction rates are doubled in the deep pre-oxidized powder compared with the combusted powder. When the superficial flow velocity is sufficiently large, a positive influence of the deep pre-oxidation is still observed on the phase transformation rates, but is compensated by the initially larger hematite content. Therefore, deep pre-oxidation does not strongly affect the total reduction time at 400 °C-500 °C. The influence of the deep oxidation treatment at higher reduction temperatures could be more significant and will be investigated in a subsequent study.

A strong influence of the oxidation treatment is observed on the microstructural evolution of the powders during the reduction process. In particular, the porosity distribution is highly heterogeneous at the end of the reduction of the combusted powder compared with the porosity distribution at the end of the reduction of the deeply oxidized combusted powder. Moreover, the increase in surface roughness favored the agglomeration of deeply oxidized particles which could be detrimental to their fluidization behavior.

Data availability

The datasets generated during and/or analyzed during the current study are available from the corresponding author on reasonable request.

CRediT authorship contribution statement

Laurine Choisez: Conceptualization, Methodology, Investigation, Formal analysis, Validation, Writing – original draft. **Kira Hemke:** Investigation. **Özge Özgün:** Investigation, Data curation. **Claudio Pistidda:** Resources, Writing – review & editing. **Henrik Jeppesen:** Writing – review & editing. **Dierk Raabe:** Writing – review & editing, Funding acquisition. **Yan Ma:** Resources, Writing – review & editing, Supervision.

Declaration of competing interest

The authors declare that they have no known competing financial interests or personal relationships that could have appeared to influence the work reported in this paper.

Acknowledgments

Supplementary materials

Supplementary material associated with this article can be found, in the online version, at doi:10.1016/j.actamat.2024.119752.

References

[1] H. Ritchie, P. Rosado, M. Roser, Emissions by sector: where do greenhouse gases come from?, Ourworldindata.Org/Ghg-Emissions-by-Sector (2020).

[2] J.M. Bergthorson, Recyclable metal fuels for clean and compact zero-carbon power, Prog. Energy Combust. Sci. 68 (2018) 169–196, https://doi.org/10.1016/j.pecs.2018.05.001.

[3] P. Julien, J.M. Bergthorson, Enabling the metal fuel economy: green recycling of metal fuels, Sustain. Energy Fuels. 1 (2017) 615–625, https://doi.org/10.1039/c7se00004a.

[4] J.M. Bergthorson, S. Goroshin, M.J. Soo, P. Julien, J. Palecka, D.L. Frost, D. J. Jarvis, Direct combustion of recyclable metal fuels for zero-carbon heat and power, Appl. Energy 160 (2015) 368–382, https://doi.org/10.1016/j.apenergy.2015.09.037.

[5] F. Patisson, O. Mirgaux, Hydrogen ironmaking: how it works, Metals. (Basel) 10 (2020) 1–15, https://doi.org/10.3390/met10070922.

[6] D. Spreitzer, J. Schenk, Reduction of iron oxides with hydrogen—A review, Steel. Res. Int. 90 (2019), https://doi.org/10.1002/srin.201900108.

[7] E. Kawasaki, J. Sanscrainte, T.J. Walsh, Kinetics of reduction of iron oxide with carbon monoxide and hydrogen, A.I.Ch.E. J. 8 (1962) 48–52.

[8] A. Bonalde, A. Henriquez, M. Manrique, Kinetic analysis of the iron oxide reduction using hydrogen-carbon monoxide mixtures as reducing agent, ISIJ Int. 45 (2005) 1255–1260.

[9] T. Murakami, Y. Kamiya, T. Kodaira, E. Kasai, Reduction disintegration behavior of iron ore sinter under high H_2 and H_2O conditions, ISIJ Int. 52 (2012) 1447–1453, https://doi.org/10.2355/isijinternational.52.1447.

[10] N.A. El-Husseiny, A. El-Amir, F.M. Mohamed, S.T. Abdel-Rahim, M.E.H. Shalabi, Kinetics of direct reduction of El-Baharia Iron ore (El-Gedida) Oasis Egypt, briquette via Hydrogen, Int. J. Sci. Eng. Res. 6 (2015) 1018–1027. http://www.ijser.org.

[11] L. Yi, Z. Huang, T. Jiang, L. Wang, T. Qi, Swelling behavior of iron ore pellet reduced by H2-CO mixtures, Powder. Technol. 269 (2015) 290–295, https://doi.org/10.1016/j.powtec.2014.09.018.

[12] H. bin Zuo, C. Wang, J. ji Dong, K. xin Jiao, R. sheng Xu, Reduction kinetics of iron oxide pellets with H_2 and CO mixtures, Int. J. Minerals. Metall. Mater. 22 (2015) 688–696, https://doi.org/10.1007/s12613-015-1123-x.

[13] A.Z. Ghadi, M.S. Valipour, S.M. Vahedi, H.Y. Sohn, A review on the modeling of gaseous reduction of iron oxide pellets, Steel. Res. Int. 91 (2020) 1900270, https://doi.org/10.1002/srin.201900270.

[14] K. He, Z. Zheng, Z. Chen, H. Chen, W. Hao, Kinetics of hydrogen reduction of Brazilian hematite in a micro-fluidized bed, Int. J. Hydrogen. Energy 46 (2021) 4592–4605, https://doi.org/10.1016/j.ijhydene.2020.10.263.

[15] S. Chen, D. Chen, Y. nan Lyu, F. bao Wu, W. ang Yin, Reduction and subsequent carburization of pre-oxidation magnetite pellets, J. Cent. South. Univ. 29 (2022) 1856–1868, https://doi.org/10.1007/s11771-022-5066-x.

[16] E.T. Turkdogan, J.V. Vinters, Gaseous reduction of iron oxides: part I. Reduction of hematite in hydrogen, Metall. Trans. 2 (1971) 3175–3188.

[17] E.T. Turkdogan, R.G. Olsson, J.V. Vinters, Gaseous reduction of iron oxides: part II. Pore characteristics of iron reduced from hematite in hydrogen, Metall. Trans. 2 (1971) 3189–3196.

[18] R.J. Fruehan, Y. Li, L. Brabie, E.J. Kim, Final stage of reduction of iron ores by hydrogen, 2005.

[19] Y. Qu, L. Xing, L. Shao, Y. Luo, Z. Zou, Microstructural characterization and gas-solid reduction kinetics of iron ore fines at high temperature, Powder. Technol. 355 (2019) 26–36, https://doi.org/10.1016/j.powtec.2019.06.048.

[20] T. Wolfinger, D. Spreitzer, H. Zheng, J. Schenk, Influence of a prior oxidation on the reduction behavior of magnetite iron ore ultra-fines using hydrogen, Metall. Materials Trans. B Process Metall. Mater. Process. Sci. 53 (2022) 14–28, https://doi.org/10.1007/s11663-021-02378-1.

[21] H. Zheng, D. Spreitzer, T. Wolfinger, J. Schenk, R. Xu, Effect of prior oxidation on the reduction behavior of magnetite-based iron ore during hydrogen-induced fluidized bed reduction, Metall. Materials Trans. B Process Metall. Mater. Process. Sci. 52 (2021) 1955–1971, https://doi.org/10.1007/s11663-021-02215-5.

[22] H. Zheng, O. Daghagheleh, T. Wolfinger, B. Taferner, J. Schenk, R. Xu, Fluidization behavior and reduction kinetics of pre-oxidized magnetite-based iron ore in a hydrogen-induced fluidized bed, Int. J. Minerals. Metall. Mater. 29 (2022) 1873–1881, https://doi.org/10.1007/s12613-022-2511-7.

[23] D. Wagner, O. Devisme, F. Patisson, D. Ablitzer, A laboratory study of the reduction of iron oxides by hydrogen, in: , 2006, pp. 111–120.

[24] A. Pineau, N. Kanari, I. Gaballah, Kinetics of reduction of iron oxides by H2. Part I: low temperature reduction of hematite, Thermochim. Acta 447 (2006) 89–100, https://doi.org/10.1016/j.tca.2005.10.004.

[25] A. Pineau, N. Kanari, I. Gaballah, Kinetics of reduction of iron oxides by H_2. Part II: low temperature reduction of magnetite, Thermochim. Acta 456 (2007) 75–88, https://doi.org/10.1016/j.tca.2005.10.004.

[26] H. Wang, B. Liu, G. Yang, C. You, Multistep kinetic study of Fe_2O_3 reduction by H_2 based on isothermal thermogravimetric analysis data deconvolution, Int. J. Hydrogen. Energy 48 (2023) 16601–16613, https://doi.org/10.1016/j.ijhydene.2023.01.201.

[27] A. El-Zoka, S. Kim, A.A. El-Zoka, L.T. Stephenson, S.H. Kim, B. Gault, D. Raabe, The fate of water in hydrogen-based iron oxide reduction, Adv. Sci. (2023) 2300626, https://doi.org/10.48550/arXiv.2301.06391.

[28] X. Zhou, Y. Bai, A.A. El-Zoka, S.H. Kim, Y. Ma, C.H. Liebscher, B. Gault, J.R. Mianroodi, G. Dehm, D. Raabe, Effect of Pore Formation on Redox-Driven Phase Transformation, Phys. Rev. Lett. 13 (2023), https://doi.org/10.1103/PhysRevLett.130.168001.

[29] M. Moukassi, P. Steinmetz, B. Dupre, C. Gleitzer, A study of the mechanism of reduction with hydrogen of pure wustite single crystals, Metall. Trans. B 14B (1983) 125–132.

[30] Q. Fradet, M. Kurnatowska, U. Riedel, Thermochemical reduction of iron oxide powders with hydrogen: review of selected thermal analysis studies, Thermochim. Acta 726 (2023), https://doi.org/10.1016/j.tca.2023.179552.

[31] C.J.M. Hessels, T.A.M. Homan, N.G. Deen, Y. Tang, Reduction kinetics of combusted iron powder using hydrogen, Powder. Technol. (2022) 117540.

[32] I.R. Souza Filho, Y. Ma, D. Raabe, H. Springer, Fundamentals of green steel production: on the role of gas pressure during hydrogen reduction of iron ores, JOM 75 (2023) 2274–2286, https://doi.org/10.1007/s11837-023-05829-z.

[33] J.O. Edström, The mechanism of reduction of iron oxides, J. Iron Steel Inst. 175 (1953) 289–304.

[34] S.H. Kim, X. Zhang, Y. Ma, I.R. Souza Filho, K. Schweinar, K. Angenendt, D. Vogel, L.T. Stephenson, A.A. El-Zoka, J.R. Mianroodi, M. Rohwerder, B. Gault, D. Raabe, Influence of microstructure and atomic-scale chemistry on the direct reduction of iron ore with hydrogen at 700°C, Acta Mater. 212 (2021), https://doi.org/10.1016/j.actamat.2021.116933.

[35] H. Zheng, O. Daghagheleh, T. Wolfinger, B. Taferner, J. Schenk, R. Xu, Fluidization behavior and reduction kinetics of pre-oxidized magnetite-based iron ore in a hydrogen-induced fluidized bed, Int. J. Minerals. Metall. Mater. 29 (2022) 1873–1881, https://doi.org/10.1007/s12613-022-2511-7.

[36] L. Choisez, N.E. van Rooij, C.J.M. Hessels, A.K. da Silva, I.R.S. Filho, Y. Ma, P. de Goey, H. Springer, D. Raabe, Phase transformations and microstructure evolution during combustion of iron powder, Acta Mater. 239 (2022), https://doi.org/10.1016/j.actamat.2022.118261.

[37] Bodil Elisabeth Monsen, Iron Ore Concentrates - oxidation and Reduction, Norwegian Institute of Technology, 1992.

[38] R.J. Longbottom, B. Ingham, M.H. Reid, A.J. Studer, C.W. Bumby, B.J. Monaghan, In situ neutron diffraction study of the reduction of New Zealand ironsands in dilute hydrogen mixtures, Mineral Process. Extract. Metall. 128 (2019) 183–192, https://doi.org/10.1080/03719553.2017.1412877.

[39] J. Jean-Philyppe, A. Fujinawa, J.M. Bergthorson, X. Mi, The ignition of fine iron particles in the Knudsen transition regime, (2023). 10.1016/j.combustflame.2023.112869.

[40] X.C. Mi, A. Fujinawa, J.M. Bergthorson, A quantitative analysis of the ignition characteristics of fine iron particles, Combust. Flame 240 (2022), https://doi.org/10.1016/j.combustflame.2022.112011.

[41] M. Auinger, D. Vogel, A. Vogel, M. Spiegel, M. Rohwerder, A novel laboratory set-up for investigating surface and interface reactions during short term annealing cycles at high temperatures, Rev. Sci. Instrum. 84 (2013), https://doi.org/10.1063/1.4817310.

[42] A.C. Dippel, H.P. Liermann, J.T. Delitz, P. Walter, H. Schulte-Schrepping, O.H. Seeck, H. Franz, Beamline P02.1 at PETRA III for high-resolution and high-energy powder diffraction, J. Synchrotron. Radiat. 22 (2015) 675–687, https://doi.org/10.1107/S1600577515002222.

[43] C. Pistidda, A. Santoru, S. Garroni, N. Bergemann, A. Rzeszutek, C. Horstmann, D. Thomas, T. Klassen, M. Dornheim, First direct study of the ammonolysis reaction in the most common alkaline and alkaline earth metal hydrides by *in situ* SR-PXD, J. Phys. Chem. C 119 (2015) 934–943, https://doi.org/10.1021/jp510720x.

[44] G. Ashiotis, A. Deschildre, Z. Nawaz, J.P. Wright, D. Karkoulis, F.E. Picca, J. Kieffer, The fast azimuthal integration Python library: pyFAI, J. Appl. Crystallogr. 48 (2015) 510–519, https://doi.org/10.1107/S1600576715004306.

[45] L. Lutterotti, Total pattern fitting for the combined size-strain-stress-texture determination in thin film diffraction, Nucl. Instrum. Methods Phys. Res. B 268 (2010) 334–340, https://doi.org/10.1016/j.nimb.2009.09.053.

[46] R.M. Cornell, U. Schwertmann, The Iron Oxides, John Wiley, 2003.

[47] H. Zheng, J. Schenk, D. Spreitzer, T. Wolfinger, O. Daghagheleh, Review on the oxidation behaviors and kinetics of magnetite in particle scale, Steel. Res. Int. 92 (2021) 2000687, https://doi.org/10.1002/srin.202000687.

[48] H. Zheng, J. Schenk, R. Xu, O. Daghagheleh, D. Spreitzer, T. Wolfinger, D. Yang, Y. Kapelyushin, Surface morphology and structural evolution of magnetite-based iron ore fines during the oxidation, Metall. Mater. Trans. B Process Metall. Mater Process. Sci. (2022), https://doi.org/10.1007/s11663-022-02475-9.

[49] M. Martin, Diffusion in Oxides, Diffusion in Condensed Matter: Methods, Materials, Models, Springer, Berlin, Heidelberg, 2005, pp. 209–247.

[50] M. Komatina, H.W. Gudenau, The sticking problem during direct reduction of fine iron ore in the fluidized bed, Metal J Metall (2004) 309–328, https://doi.org/10.30544/378.

[51] O. Levenspiel, Chemical Reaction Engineering, John Wiley & Sons, 1998.

[52] S. Vyazovkin, A.K. Burnham, J.M. Criado, L.A. Pérez-Maqueda, C. Popescu, N. Sbirrazzuoli, ICTAC Kinetics Committee recommendations for performing kinetic computations on thermal analysis data, Thermochim. Acta 520 (2011) 1–19, https://doi.org/10.1016/j.tca.2011.03.034.

[53] A. Khawam, D.R. Flanagan, Solid-state kinetic models: basics and mathematical fundamentals, J Phys Chem B 110 (2006) 17315–17328, https://doi.org/10.1021/jp062746a.

[54] Y. Bai, J.R. Mianroodi, Y. Ma, A.K. da Silva, B. Svendsen, D. Raabe, Chemo-mechanical phase-field modeling of iron oxide reduction with hydrogen, Acta Mater. 231 (2022), https://doi.org/10.1016/j.actamat.2022.117899.